LAWRENCE
LIVERMORE
NATIONAL
LABORATORY

LLNL-PROC-646682

Localized planarization of optical damage using laser-based chemical vapor deposition

M. J. Matthews, S. Elhadj, G. M. Guss, A. Sridharan, I. L. Bass, N. D. Nielsen

November 21, 2013

SPIE Laser Damage 2013
Boulder, CO, United States
September 22, 2013 through September 25, 2013

Disclaimer

temperature was raised again to anneal the deposited silica and increase the damage threshold. In order to fill a specified volume of a pre-measured pit, calibration curves of both volume and deposition width were produced over a range of laser operating parameters (beam size, power and exposure time). Final morphology was assessed using laser confocal scanning microscopy and scanning electron microscopy.

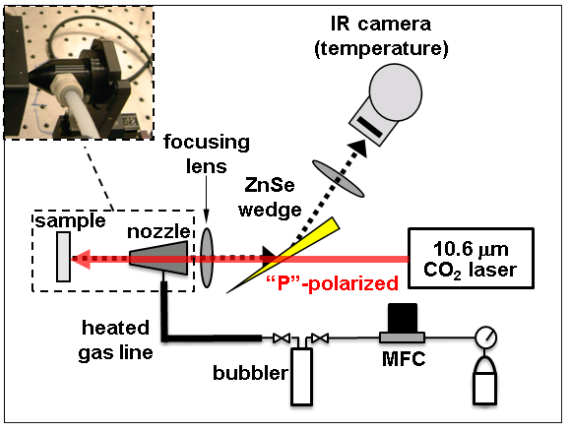

Figure 2. Experimental setup for laser-based chemical vapor deposition of silica. A 10.6 μm laser light is directed through a focusing lens and optically-coupled flow nozzle to focus at the test sample. Tetraethylorthosilicate contained in a bubbler is sent via carrier gas to the nozzle and flows over the test sample, decomposing at the laser heated surface. A calibrated IR camera (described in Ref. 5) is used to measure laser-driven temperature changes along the test sample surface.

2.2 In situ temperature measurements

Detection of long wave IR radiation was achieved using a liquid nitrogen cooled Mercury Cadmium Telluride (MCT) camera capable of detecting radiation within the 2 to 12 μm range (see Fig. 2). The MCT camera uses a 256×256 element focal plane array with 40 μm square pixel. Thermal background from the surroundings was removed with the 8.9 μm centered bandpass filter by including the filter as part of the cold shield installed in front of the focal plane array. As shown in Fig. 2, a 10.6 μm laser (Synrad firestar V20), with a maximum output power of 20 watts and power stability of ±5%, is used for heating the fused silica sample. The laser beam is collimated with a pair of lenses, and passed through a variable magnification afocal telescope to a 10" focal length final focusing lens. By varying the magnification of the afocal telescope, the collimated beam size at the entrance to the final focusing lens could be adjusted so that the laser spot size on the fused silica surface was varied between 250 μm and 1000 μm without changing the focal location. Laser beam size was measured using the standard knife edge technique in coordination with the sample plane power meter. An un-coated ZnSe wedged plate, inserted before the final focusing lens, is oriented at Brewster's angle (67.4°) to pass the p-polarized 10.6 μm laser light while reflecting 50% of the 'S' polarized fraction of the black body emission collected from the heated surface by the final focusing lens. Since the black body emission is un-polarized, only a quarter of the emitted black body radiation collected is sent to the thermal camera. Given a f/# of 5 for the thermal camera imaging setup, a lateral spatial resolution of better than 200 μm can be achieved. Average laser power was measured at the sample plane before measurements using a standard IR optical power meter. Laser beam size was measured using a beam profiler (Pyrocam III, Spiricon, Grosshansdorf, Germany). The duration of the laser exposure ranged from 10 to 1000 seconds. All experiments were conducted in ambient air. Additional details can be found in Ref. 5.

2.3 Real time phase shifting interferometry

Alignment of the initial damage or pre-fabricated pit with the L-CVD laser beam is crucial to proper shape control. We use real time phase-shifting interferometry (RT-PSDI) to detect the thermal deflection caused by mild laser heating and align this symmetric bulge in the surface of the pit to be filled. The RT-PSDI measurement system consists of a Michelson interferometer utilizing a 532 nm continuous wave laser source (Millennia, Spectra-Physics). One leg of the interferometer is manually adjustable to compensate for large phase differences between the two legs. The other leg is attached to a piezoelectric driver which can vary the phase over one wavelength in a

designed ramp. Each leg of the interferometer is launched into a single mode fiber and passes through a fiber polarization adjuster. The interferometer is setup on a separate vibration isolated table and is optically-coupled to the L-CVD table where the cleaved fiber ends are held in a fixture. The fixture stacks the fiber ends vertically and allows for adjusting their separation and alignment verses a vertical line. The light from the fibers passes through the transparent sample from the backside, reflects off the surface under study, and continues to the camera where an interferogram is captured. A computer software program is used to capture 12 interferograms during each ramp of the piezo. The phase shift from the piezo is assigned to each interferogram. Each pixel in the interferogram when plotted verses phase is a sinusoidal function and the software uses a numerical algorithm to retrieve the amplitude and phase shift of the curve. The phase shift can then be compared between pixels to determine differences in height of the surface profile. Additional details of the RT-PSDI apparatus can be found elsewhere.[5]

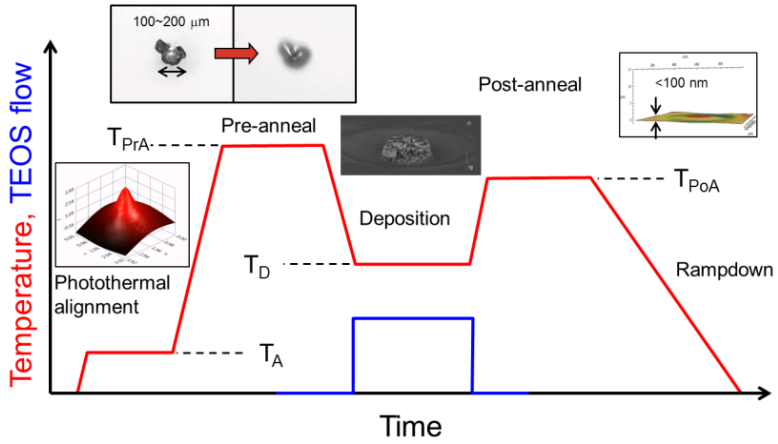

Figure 3. Diagram showing the heating schedule used for in-filling damage sites.

3. RESULTS AND DISCUSSION

Because the deposition rates must be sufficient to infill expected damage site depths of 50-300 μm over reasonable timescales (~minutes), a survey of deposition rate was first performed. Figure 4 displays our measured deposition rates as a function of peak temperature (closed symbols) as compared to several other depositions using molecular beam epitaxy, sputtering and e-beam evaporation methods (open symbols). As shown, rates as high as ~22 μm/min were achieved, due in large part to the high temperatures (>1000 K) and 3D diffusion processes accessible to laser-based CVD. Typical deposition rates used were approximately 10 μm/min in order to avoid unwanted morphological effects known to occur in L-CVD profiles.[6] Therefore, our damage in-filling technique can replace material lost within typical damage sites over 5 to 30 min, with a total processing time (including alignment and annealing) of about 20 to 45 min. The spread in the growth rate data is due to two factors. For one, because we use an air-cooled CO2 laser, there was considerable power fluctuation when operating in 'open loop' during deposition rate measurements. Subsequent in-filling experiments used a closed loop, feedback system which stabilized the laser power. Secondly, for the very high rates an irregular morphology was observed which affected the peak height measurement used to evaluation the growth rate.

We have previously presented the analysis of laser-based thermal annealing of silane-based 'bulk' CVD films, showing that, with sufficient annealing temperature and time the damage threshold of deposited films can exceed that of today's best etched surfaces.[7] To assess the damage threshold of our L-CVD material, a 36-site sample was produced which could be 351 nm, 5-ns pulse laser damage tested in our Optical Sciences Laser damage test facility.[8] The results are displayed in Table 1, along with data for laser-grown damage sites (~150 μm in diameter) and data from our previous study.[9] Although our primary study involved TEOS-based silica, we included data using a silane precursor which will be explored further in a future study.[4] Interestingly, the initial damage threshold was ~5 J/cm^2 regardless of the type of deposition or whether it was deposited silica or damaged material. Upon annealing at 1600

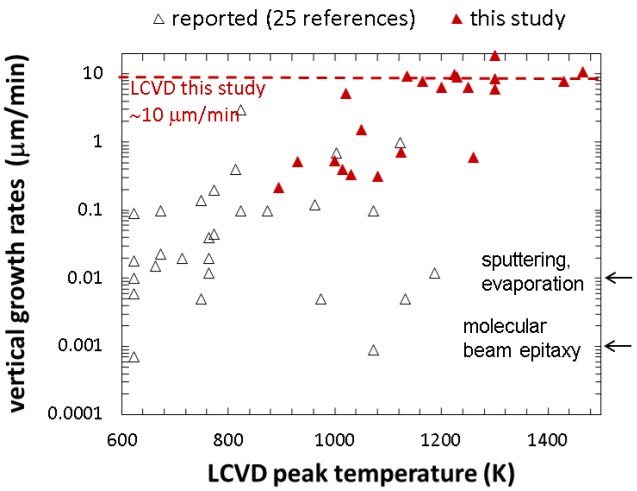

Figure 4. Measured deposition rates using L-CVD as compared to published results using other methods.

K for 60 s using a CO_2 laser for heating in all cases, the damage threshold increases substantially with the damage site increasing to ~7 J/cm^2 and the CVD materials increasing to between 6 and 10 J/cm^2. Higher temperature treatments produced thresholds in excess of 12 J/cm^2 and in some cases no damage was observed. Notably, this latter number is well above the operating conditions (8-9 J/cm^2) typical in ICF laser systems.[10] These measurements further confirm the notion that, in spite of the starting point of the defective silica, the damage threshold can be enhanced with sufficient laser thermal annealing.

Table 1. 351 nm, 5 ns pulsed laser damage threshold measurements (PE=plasma enhance).

	Damage site (J/cm^2)	**TEOS-based L-CVD silica** (J/cm^2)	**Silane-based L-CVD silica** (J/cm^2)	**PE-CVD silica film**[9] (J/cm^2)
Pre-annealed	4.9 ± 0.4	4.6 ± 0.4	5 ± 1	~5
1600 K, 60s annealed	7.2 ± 1.9	10.7 ± 0.8	6 ± 1	~10

Turning now to morphological evaluation of our in-filled sites, we present in Fig. 3 laser scanning confocal profilometry before and after in-filling. The initial site was prepared by first evaporating away material[11] to enhance reproducibility, although direct in-filling of pre-annealed damage sites was also demonstrated. As shown in the figure, a ~7 μm deep pit was successfully registered to our L-CVD laser beam and material within the pit (~2.2x10^5 μm^3) was replenished leaving a ~100 nm feature in the center. Although care was taken to closely match the deposition profile with the conjugate of the pit profile, a perfectly flat surface was not achieved. In fact, the total volume of the final site was negligible, and the morphology was fairly symmetric. However, as we study in more detail in the next section, the deposition shape differed from that of the pit conjugate slightly, yielding a characteristic castle/moat structure observed.

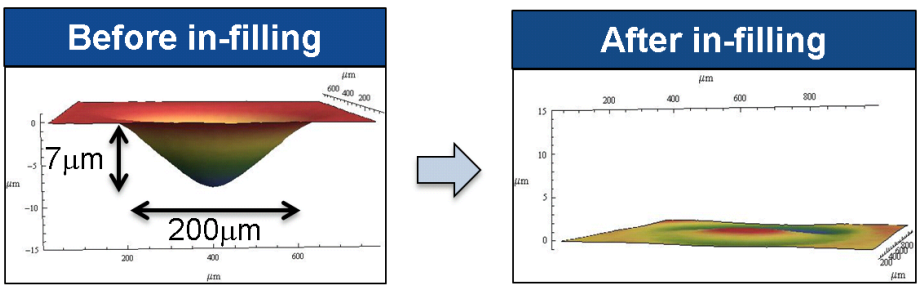

Figure 5. Measured height profile of a 7 μm deep pit in silica before and after application of L-CVD mitigation.

4. PROPAGATION ANALYSIS

Along with a high damage threshold to pulsed UV laser light and reasonable deposition rates, L-CVD in-filled sites must leave the treated surface sufficiently flat as to not produce focusing effects downstream. Fourier optical theory was used to describe the propagation and interaction of incident light associated with L-CVD depositions. In addition, we analyzed idealized deposition profiles to study the various tolerances in our experimental system. Diffraction due to localized surface protrusions and depressions can lead to light intensification, which can be characterized by simulating the effective phase imprinted on the optic surface. Sites were sampled using a laser scanning confocal microscope (Keyence VX-100) with ~500 nm lateral resolution and ~10 nm axial resolution. The height maps were then used to calculate phase maps assuming an index change of -(n-1)=-0.46 going from air to glass. A 1024x1024 pixel grid with 1 μm/pixel resolution was used to construct a 1x1 mm square, 12th order super-Gaussian complex field with unity intensity, to which phase maps were added at the initial propagation position (z=0). Generally the intensification properties of the final sites followed closely the behavior in pit morphology. Because the final heights formed from L-CVD infilling are small compared with the lateral dimension, the diffraction angles are also small. Thus, we use the Fresnel approximation to express the optical transfer function to propagate over 200 mm in Δz = 1 mm steps as [12]

$$H(\omega_x, \omega_y) \approx \exp(-ik\Delta z)\exp[-i\pi\lambda\Delta z(\omega_x^2 + \omega_y^2)] \quad (1)$$

where ω_x, ω_y are the plane wave x and y spatial frequencies. Using either experimentally determined height-derived phase maps or simulated ones we construct initial field distributions and calculate the propagated complex field using fast Fourier transforms (FFTs).

Figure 6 shows simulated surface profiles (a-c) created by various errors in the deposition process and the resulting peak-to-mean intensities (d-f) using our propagation analysis. In each case an idealized initial (annealed) damage pit is modeled by a Gaussian (amplitude = 10 μm, standard deviation = 150 μm) whereas the deposition profile is modeled as its inverse with a specified perturbation. In Fig. 6(a,d) the deposition profile has an amplitude error of -1 μm resulting in an under-fill, Fig. 6(b,e) correspond to a (1σ) width error of 13 μm and Fig. 6(c,f) correspond to a

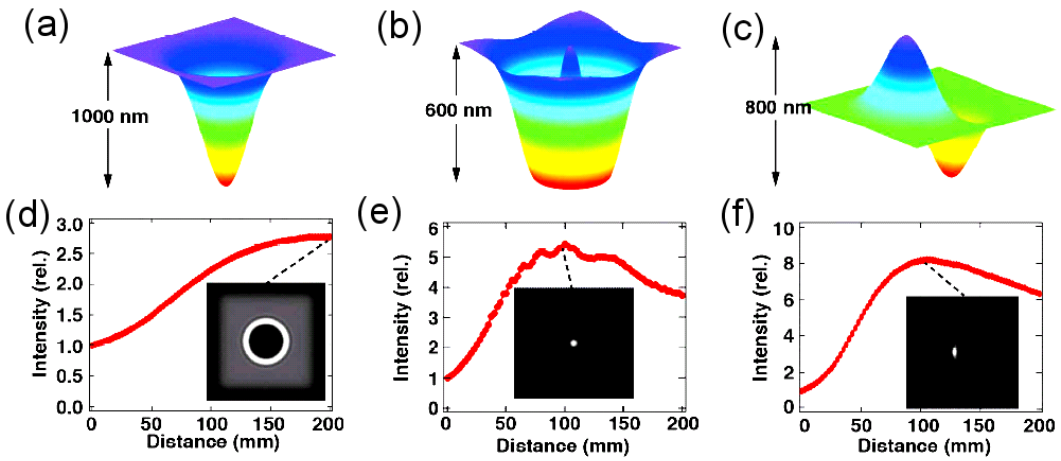

Figure 6. Simulated surface profiles (a-c) created by errors in the deposition process and the resulting peak-to-mean intensities (d-f) using our propagation analysis. In each case an idealized initial (annealed) damage pit is modeled by a Gaussian (amplitude = 10 μm, standard deviation = 150 μm) whereas the deposition profile is modeled as its inverse with a specified perturbation. For example, in (a,d) the deposition profile has an amplitude error of -1 μm resulting in an under-fill, (b,e) correspond to a (1σ) width error of 13 μm and (c,f) correspond to a registration (centering) error of 10 μm. The insets to (d)-(f) display the field intensity over the 1x1 mm grid at the propagation distance indicated.

registration (centering) error of 10 μm. Generally, an under-fill with perfect alignment and deposition width matching produced the lowest intensification [Fig. 6(a,d)], while the corresponding over-fill produced the highest (not shown). Similarly, over-matching the conjugate pit profile produced lower intensification than under-matching because the latter yields a lens-like feature in the center of the final profile [Fig. 6(b,e)]. Referring back to Fig. 5,

we see that the profile yielded in that particular deposition was likely the result of an under-matched deposition profile. Finally, a mis-alignment of the deposition with the pit center always resulted in a lens-like feature, and hence high intensification, regardless of the direction of the shift.

Although high peak intensifications could result from the aforementioned errors, it is worth noting that this increase in and of itself does not produce an ineffective in-fill relative to a pre-annealed-only damage site. That is, the likelihood of damage depends not only on intensification levels but also on where the next optic downstream is placed from the mitigation site. Figure 6 shows the propagated peak-to-mean intensification of a pre-deposition annealed damage site pit ('pit', original damage site diameter 100 μm), compared with that of the final, in-filled and annealed mitigation site ('fill'). While the in-filled site produces greater intensification between 0 and 10 mm, there is a slight reduction over the initial melt-only site over the range 12 to 33 mm. Thus, for an optic of sufficient thickness, such as a focusing lens in an ICF laser system (10 to 40 mm thick) the peak intensification of the in-filled site will occur in the optic bulk and not at the damage-prone output surface. We can conclude then that, while perfect infilling is ultimately desired, the ability to additively modify the surface features around a damage pit can be used to shift the intensification maximum to propagation distances that are more desirable in terms of damage likelihood.

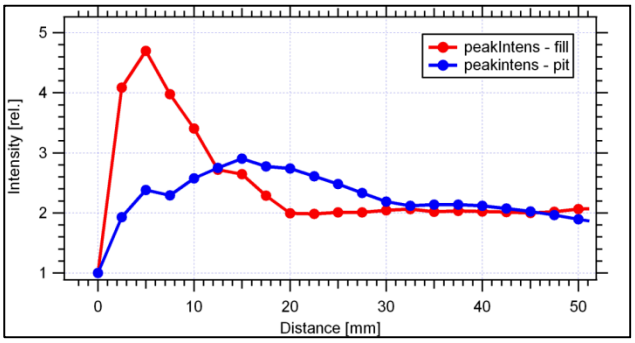

Figure 6. Propagated peak-to-mean intensification of a pre-deposition annealed damage site pit ('pit', original damage site diameter 100 μm), compared with that of the final, in-filled and annealed mitigation site ('fill').

5. DEPOSITION MODEL

To accurately predict both surface morphology and overall deposition rates in a nozzle-driven L-CVD system we solve a fully-coupled set of mass transport, thermal transport and chemical reaction equations using COMSOL Multiphysics finite element analysis software. Laser heating is simulated separately by first solving the steady state laser-heat transport equation and imposing the surface temperature profile as a fixed boundary condition on the fluid domain. TEOS vapor diluted in a carrier gas (air) is brought to the laser-heated surface by way of a nozzle, as shown in Fig. 1. Finite element methods are used to solve for fluid temperature, pressure, velocity and chemical species concentration. A two-step reaction pathway is assumed where an intermediate is first formed through decomposition of the silica precursor (TEOS) in the gas phase, which then transports and reacts at the surface under a separate chemical kinetic rate equation.[13, 14] Although the decomposition of TEOS in various environments is known to involve several reaction pathways, we further simplify our model by neglecting details of the radical formation kinetics and volatile species reaction, and simply express the dominant first order reactions as:

$$Si(OC_2H_5)_4 \xrightarrow{T>600^oC} SiO_2 + byproducts. \tag{2}$$

Note that the reactions above are taken to be irreversible and that the byproducts under similar operating conditions will include several alky- and hydroxyl-rich species such as ethane, ethanol and diethylether $O(C_2H_5)_2$ (DEE).[15] For the purposes of the simulation we select to model the byproducts as only the DEE, since the exact identity of the byproducts will not significantly affect either the deposition kinetics or the prediction of deposition rates. The reaction rate equation for the decomposition of TEOS is expressed in terms of an Arrhenius activation energy expression,

$$R_{TEOS} = c_{TEOS} k_0 e^{-E_a/k_B T} = -R_{SiO_2} = \tfrac{1}{2} R_{DEE} \tag{3}$$

where c_{TEOS} is the concentration of TEOS (0.0834 mole/m^3), k_0 is the reaction rate pre-factor (4.9x10^{13} s^{-1}) and E_a is the activation energy (~200 kJ/mole). The reaction of the gas-phase reacted intermediate SiO_2 species is described in terms of a temperature-independent sticking probability.[16] The fluid flow and mass transport were modeled assuming a 3 mm diameter gas nozzle aperture, gas superficial velocity of ~1 m/s (0.6 L/min) and nozzle orifice to substrate distance of 8 mm. The calculated Reynolds's number for our geometry and assuming an ideal gas was found to be approximately 10 to 100 over the range of temperatures studied here (room temperature to 2000 K). Therefore, we assumed laminar flow of a compressible gas and solve the Navier-Stokes and continuity equations given by:

$$\rho\left(\frac{\partial \vec{u}}{\partial t} + \vec{u}\cdot\vec{\nabla}\vec{u}\right) = -\vec{\nabla}p + \vec{f} + \vec{\nabla}\cdot\vec{\mathrm{T}} \tag{4}$$

$$\frac{\partial \rho}{\partial t} + \vec{\nabla}\cdot(\rho\vec{u}) = 0 \tag{5}$$

where ρ, u and p are the fluid density, velocity and pressure, respectively. In Eq. (4), f represents the volumetric body force acting on the fluid while T is the deviatoric component of the total stress tensor. Buoyancy driven flow and natural convection are neglected. Because the TEOS vapor is produced by bubbling a carrier gas through a bubbler at low temperatures, we assume a dilute (<10%) mixture of TEOS precursor and resulting decomposition products which diffuse according to Fick's law. Furthermore, because of the low concentrations of TEOS and its decomposition products, temperature-dependent expressions for ρ are derived from known values for air using the ideal gas law. The mass transport equation for each species i of concentration c_i with a volumetric reaction rate source term R_i and mass diffusivity D_i is given by

$$\frac{\partial c_i}{\partial t} + \vec{\nabla}\cdot(-D_i\vec{\nabla}c_i) + \vec{u}\cdot\vec{\nabla}c_i = R_i \tag{6}$$

where R_i is derived through Eq.(3). Under assumption of dilute species diffusion (concentrations in air less than ~10%), concentration independent diffusivities were used with D_{TEOS}=10^{-6} m^2/s, D_{DEE}=10^{-5} m^2/s and D_{SiO2}=10^{-8} m^2/s. The volatile species diffusivities (TEOS, DEE) were estimated using Chapman-Enskog theory, while the SiO_2 intermediate diffusivity was estimated assuming a oligomer/nanoparticle size of ~10 nm.

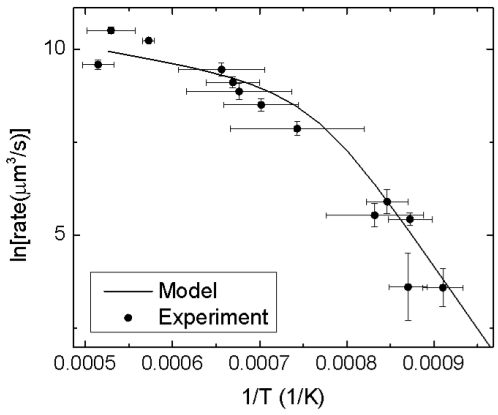

Figure 7. Measured (log) deposition rates as a function of inverse temperature compared to predicted rates using the deposition model presented in the text.

Predicted deposition rates are displayed in Fig. 7 along with measured deposition rates for a range of deposition parameters (1/e^2 diameter of ~800 μm, deposition times 30 - 180 s, laser power 1 – 4 W). Excellent agreement is found using literature values for the reaction rate parameters. In particular, we predict the well-known roll-over of reaction rates as a function of 1/T occurs at ~7.5x10^{-4} K^{-1} (~1300 K) associated with a transition from transport- (high T) to kinetic-limited behavior in L-CVD systems.[1] Because the high temperature, transport limited regime also corresponds to more irregular surface morphology, our simulations can serve as a guide to optimizing deposition rates while preserving well-behaved deposition profiles. Further details of our study of deposition kinetics and morphology will be published elsewhere.[17]

6. CONCLUSIONS

Experimental results and simulations of a novel additive approach towards damage mitigation were presented. Our method consists of locally depositing silica using laser-based chemical vapor deposition (L-CVD) in open air to produce damage resistant in-filled material with minimal surface perturbations. A CO_2 laser is used to heat damaged regions under controlled flow and composition to achieve a thermally activated polymerization of the tetraethylorthosilicate (TEOS) precursor to form silica. The protocol for in-filling mitigation consisted of a photothermal alignment procedure using a real time interferometer, a pre-deposition anneal step, followed by deposition and a final anneal of deposited material. Measured deposition rates as a function of temperature agree well with a heterogeneous phase model implemented using finite element methods. Successful application of such a method could reduce processing costs, extend optic lifetime, and lead to more damage resistant laser optics used in high power applications.

Acknowledgements

S. Elhadj and M. Matthews kindly acknowledge support from UCFR grant #12-LR-237713. This work was performed under the auspices of the U.S. Department of Energy by Lawrence Livermore National Laboratory under Contract DE-AC52-07NA27344. LLNL-PROC-646682

REFERENCES

[1] C. Duty, D. Jean and W. J. Lackey, Int. Mater. Rev. **46** (6), 271-287 (2001).
[2] J. Mazumder and A. Kar, *Theory and application of laser chemical vapor deposition*. (Springer, 1995).
[3] D. Bäuerle, *Laser Processing and Diagnostics*. (Springer-Verlag Berlin, 1983).
[4] S. Elhadj, To be published.
[5] G. Guss, To be published.
[6] A. J. Silvestre, M. J. Santos and O. Conde, Key Eng Mat **230-2**, 56-59 (2002).
[7] M. J. Matthews, N. Shen, S. Elhadj, P. E. Miller, A. J. Nelson, T. A. Laurence and J. Hamilton, Laser-Induced Damage in Optical Materials: 2012 **8530** (2012).
[8] M. C. Nostrand, T. L. Weiland, R. L. Luthi, J. L. Vickers, W. D. Sell, J. A. Stanley, J. Honig, J. Auerbach, R. P. Hackel and P. J. Wegner, SPIE **5273**, 325-333 (2003).
[9] N. Shen, M. J. Matthews, S. Elhadj, P. E. Miller, A. J. Nelson and J. Hamilton, J Phys D Appl Phys **46** (16) (2013).
[10] C. A. Haynam, P. J. Wegner, J. M. Auerbach, M. W. Bowers, S. N. Dixit, G. V. Erbert, G. M. Heestand, M. A. Henesian, M. R. Hermann, K. S. Jancaitis, K. R. Manes, C. D. Marshall, N. C. Mehta, J. Menapace, E. Moses, J. R. Murray, M. C. Nostrand, C. D. Orth, R. Patterson, R. A. Sacks, M. J. Shaw, M. Spaeth, S. B. Sutton, W. H. Williams, C. C. Widmayer, R. K. White, S. T. Yang and B. M. Van Wonterghem, Appl. Opt. **46** (16), 3276-3303 (2007).
[11] I. L. Bass, G. M. Guss, M. J. Nostrand and P. J. Wegner, in *Laser-Induced Damage in Optical Materials: 2010* (Proceedings of SPIE-The International Society for Optics and Photonics, Boulder, CO, USA, 2010), Vol. 7842, pp. 784220.
[12] B. E. A. Saleh and M. C. Teich, *Fundamentals of Photonics*. (John Wiley & Sons, Inc., New York, NY, 1991).
[13] S. B. Desu, Journal of the American Ceramic Society **72** (9), 1615-1621 (1989).
[14] M. E. Coltrin, P. Ho, H. K. Moffat and R. J. Buss, Thin Solid Films **365** (2), 251-263 (2000).
[15] L. L. Tedder, G. Q. Lu and J. E. Crowell, J. Appl. Phys. **69** (10), 7037-7049 (1991).
[16] M. E. Bartram and H. K. Moffat, J Vac Sci Technol A **14** (3), 872-878 (1996).
[17] M. J. Matthews, To be published.